ELSEVIER

Numerical simulation of vortex-shedding phenomenon in a channel with flow induced through porous wall

D. Couton and S. Doan-Kim
Laboratoire d'Etudes Thermiques, Ecole Nationale Supérieure de Mecanique et d'Aérotechnique, Site du Futuroscope, France

F. Vuillot
Direction de l'Energétique, Office National d'Etudes et de Recherches Aérospatiales, Fort de Palaiseau, Palaiseau, France

Segmented solid propellant rocket motors tend to develop unpredicted pressure and thrust oscillations that could be attributed to a periodic phenomenon. An experimental and numerical assessment of the stability of a solid propellant motor was conducted. This numerical computation was based on an experimental study carried out on a cold-flow, reduced-scale, bidimensional duct with a complex internal geometry (obstacles, outflowing cavities, submerged nozzle). The objectives of our study are to characterize the internal flow (mean, fluctuating induced by injection through a porous wall and the shear layer created at the top of the second obstacle. The code employed solves the unsteady, compressible two-dimensional (2-D) Navier–Stokes equations in a laminar regime by a predictor-corrector MacCormack scheme. Three grids are developed for the evaluation while respecting the complexity of the internal geometry. The results obtained allow us to separate the flow into two zones: one, laminar, upstream of the obstacle; the other, disturbed, downstream, in which vortex structures develop. The phenomena of instabilities (vortex-shedding, pairing) are in accordance with the first two acoustic longitudinal modes of the chamber. Last, the numerical computations are discussed and systematically compared with the experimental results.

Keywords: channel cold-flow; wall injection; hydrodynamic instabilities; vortex shedding

Introduction

This work is part of a study concerning the evaluation of combustion stability on a segmented solid propellant rocket motor. The segmentation of the solid propellant, because of the concept of the booster, generates a significant potential risk of instability, even if the calculations based on conventional linear acoustics allow us to predict that this motor is stable. Significant pressure and thrust oscillations have been reported (Mason et al. 1979; Mathes 1980; Dunlap and Brown 1981; Brown et al. 1985), which were unpredicted, at frequencies close to the first longitudinal modes. Recently, analyses of the full-scale firing results of the pressure oscillations have been reported (Scippa et al. 1994). These oscillations could be attributed to a periodic vortex-shedding phenomenon attributable to a solid coupling between the instabilities of the shear layer and the acoustic field of the chamber. Therefore, vortex-shedding occurs, because the segmentation of the propellant blocks generates highly sheared zones. These zones are created either in the discontinuities of the propellant blocks or in the protuberances of rigid inhibitors.

In this context, a number of experimental arrangements of simulation in cold flow have been conducted (Dunlap et al. 1990; Culick and Magiawala 1979; Isaacson and Marshall 1982; Hourigan et al. 1990). Information on both flow characteristics and on vortex-shedding is given. In most experiments, at least one pair of diaphragms are considered to be necessary to promote vortex shedding. These arrangements show that the instabilities are generated by flow shearing at the first obstacle. The presence of a second obstacle, or one such as a submerged nozzle, can trigger the feedback phenomenon when the flow vortices collide with the second obstacle (Flatau and Vanmoorhem 1990). One single diaphragm at a strong shear zone, however, is sufficient to generate a vortex-shedding phenomenon. In this case, the feedback is generated on the second obstacle. This could be what occurs with the full-scale motor (Figure 1): immediately at firing, two obstacles appear and become more and more protuberant as the propellant blocks are consumed. Rapidly, however, (i.e., after

Address reprint requests to Dr. S. Doan-Kim, Laboratoire d'Etudes Thermiques, Ecole Nationale Supérieure de Mécanique et d'Aérotechnique, Site du Futuroscope 86906 BP 109 Cedex, France.

Received 13 March 1996; accepted 8 August 1996

Int. J. Heat and Fluid Flow 18: 283–296, 1997

655 Avenue of the Americas, New York, NY 10010

0142-727X/97/$17.00
PII S0142-727X(97)00005-2

the firing phase) only one obstacle, the second, hinders the development of the burnt gases, before they reach the submerged nozzle in the aft end.

Recent works have demonstrated that a complete simulation of the compressible internal unsteady flow with Euler or Navier–Stokes programs is feasible in the case of a simple test of a solid propellant rocket motor (Vuillot 1991; 1992). These computations can be performed in either axisymmetric or two-dimensional (2-D) planar geometry. The instabilities of the shear layer are well reproduced. Qualitatively, they seem to be in good agreement with experimental results obtained with small-scale motors: the frequencies of instabilities change but remain close to the first longitudinal modes (Vuillot 1993). However, the authors observe that the self-maintained vortex-shedding fixates on the second acoustic mode instead of on the first one, as was expected, probably because of the strong coupling with the acoustics of the chamber. Such a simulation, which constitutes one of the very first in the domain of complete numerical simulations, demonstrates that a direct numerical capture of the phenomenon of vortex-shedding is feasible in a simple test case.

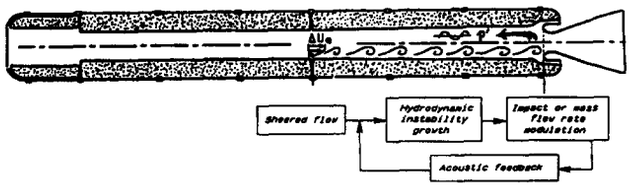

Figure 1 Illustration of the possible phenomenon of vortex shedding in a segmented solid propellant rocket motor

The present work is divided into three parts. First, the numerical computations performed in a complex internal geometry that takes into account the internal cavities, two prominent diaphragms, a submerged nozzle plus given boundary conditions, particularly the injection walls, are presented. The computations, conducted on specific grids, allow us: 1) to obtain a description both in steady (Mean flow organization section) and unsteady (Hydrodynamic instability section) states of the internal flow generated by injection through porous walls; 2) to describe the creation and the development of the shear layer; and 3) to estimate the risks of instabilities as well as their links to the chamber acoustics. The numerical results are compared to the experimental results obtained in a cold-flow model. The main purpose of the work is to understand the fundamental phenomena responsible for the development of the shear layer downstream of the obstacle and of the coupling between confined hydrodynamic instabilities and the acoustic field.

The computational code

Numerical scheme

The numerical program used is the SIERRA code (Unsteady Simulation of Flows and Acoustic Reputed Regimes) of the ONERA. It allows us to solve the unsteady two-dimensional (2-D), compressible Navier–Stokes equations in a laminar regime. The equations are written in conservative vector form for a 2-D planar geometry.

$$\iint_{\Omega} \frac{\partial \mathbf{U}}{\partial t} \cdot \mathrm{d}\Omega = -\oint_{S1 \text{ to } 4} \left[\{\vec{\mathbf{F}} i + \vec{\mathbf{G}} j\} \cdot \vec{\mathbf{n}} \right] \mathrm{d}S \qquad (1)$$

Notation

a_0	speed of sound, m/s
CF	Fourier coefficient
Cp	constant pressure specific heat
Cv	constant volume specific heat
E	total energy per unit of mass, J/kg
f	frequency, Hz
f_{1L}	first acoustic longitudinal mode, Hz
h_c	height of channel, m
h_t	height of throat, m
L	length of channel, m
$\dot{m}$	injected mass flow, kg/s
$\mathrm{M} = u/a_0$	mean longitudinal Mach number
Pr	Prandtl number
p_{he}	head-end pressure, Pa
p	mean pressure, Pa
p'	fluctuating pressure, Pa
r	perfect gas constant, J/kg·K
Re_a	axial Reynolds number
Re_i	injection Reynolds number
$\mathrm{St} = f_{1L} \cdot h_c / u_c$	Strouhal number
$s = -10 \cdot \log(\mathrm{p}/r^{\gamma})$	pseudoentropy
t	time, s
T	ambient temperature, K
T_{527}	527 Hz frequency signal period, s
u	mean longitudinal velocity, m/s
u_c	channel mean longitudinal velocity, m/s
$u_{\max}$	maximum longitudinal velocity of shear layer, m/s
u'	fluctuating longitudinal velocity, m/s
v	mean transverse velocity, m/s
x	axial coordinate, m
$X = x/L$	normalized axial coordinate
y	transverse coordinate, m
$Y = y/h_c$	normalized transverse coordinate

Greek

α	artificial viscosity parameter
γ	specific heat ratio
δ	shear layer thickness, m
ΔP	pressure deviation, Pa
ΔU	velocity deviation, m/s
Δu_e	velocity deviation in shear layer, m/s
κ	thermal conductivity
μ	dynamic laminar viscosity, kg/m·s
ρ	density, kg/m^3
$\tau_u = \sqrt{\overline{u'^2}}/u$	local turbulence rate
υ	kinematic viscosity, m^2/s
ω	pulsation, rad/s
$\Omega = (\partial v/\partial x) - (\partial u/\partial y)$	rotational, s^{-1}

with

$$\mathbf{U}=\begin{bmatrix}\rho\\ \rho u\\ \rho v\\ \rho E\end{bmatrix},\qquad \mathbf{F}=\begin{bmatrix}\rho u\\ \rho u^2+\sigma_x\\ \rho uv+\tau_{xy}\\ (\rho E+\sigma_x)u+\tau_{yx}v+\Phi_x\end{bmatrix},$$

$$\mathbf{G}=\begin{bmatrix}\rho v\\ \rho uv+\tau_{yx}\\ \rho v^2+\sigma_y\\ (\rho E+\sigma_y)v+\tau_{xy}u+\Phi_y\end{bmatrix} \tag{2}$$

where

$$\sigma_x=p-\lambda\cdot\left(\frac{\partial u}{\partial x}+\frac{\partial v}{\partial y}\right)-2\mu\frac{\partial u}{\partial x},$$

$$\sigma_y=p-\lambda\cdot\left(\frac{\partial u}{\partial x}+\frac{\partial v}{\partial y}\right)-2\mu\frac{\partial v}{\partial y}$$

$$\tau_{xy}=\tau_{yx}=-\mu\left(\frac{\partial u}{\partial y}+\frac{\partial v}{\partial x}\right),\qquad \Phi_x=-\kappa\frac{\partial T}{\partial x},\qquad \Phi_y=-\kappa\frac{\partial T}{\partial y}$$

and

$$\lambda=-\frac{2}{3}\mu,\qquad E=c_vT+\frac{(u^2+v^2)}{2}\qquad\text{and}\qquad \mathrm{Pr}=\frac{\mu c_p}{\kappa}$$

The equations are directly discrete in the physical space and are solved by means of an explicit predictor-corrector MacCormack scheme in finite volume formulation. The solution at the center of grid cell (i,j) at time $(n+1)\Delta t$ is calculated in two steps from the flux balance through grid cell sides in the following way.

$$\mathbf{U}_{i,j}^{n+1}=\mathbf{U}_{i,j}^{n}-\Delta t\cdot\sum_{k=4\text{ sides}}\left[\mathbf{F}_k^{\pm}\cdot\frac{S_k}{V(i,j)}\vec{\mathbf{n}}_k\cdot\vec{\mathbf{i}}_x+\mathbf{G}_k^{\pm}\cdot\frac{S_k}{V(i,j)}\vec{\mathbf{n}}_k\cdot\vec{\mathbf{i}}_y\right]^n \tag{3}$$

$$\mathbf{U}_{i,j}^{n+1}=\frac{1}{2}\left\{\mathbf{U}_{i,j}^{n}+\mathbf{U}_{i,j}^{n+1}-\Delta t\cdot\sum_{k=4\text{ sides}}\left[\mathbf{F}_k^{\pm}\cdot\frac{S_k}{V(i,j)}\vec{\mathbf{n}}_k\cdot\vec{\mathbf{i}}_x+\mathbf{G}_k^{\pm}\cdot\frac{S_k}{V(i,j)}\vec{\mathbf{n}}_k\cdot\vec{\mathbf{i}}_y\right]^{n+1}\right\} \tag{4}$$

where k is a summation index that indicates the four grid cell sides. Superscripts + and − indicate forward and backward flux expressions. The ± sequence is alternated at each time-step. Indices i,j indicate the spatial discretization, and $V(i,j)$ correspond to the volume of the cell.

To improve the stability of numerical scheme and to dissipate numerical oscillations, dissipation terms are added to the scheme using the algorithm of artificial viscosity defined by Jameson and Schmidt (1981). Their method consists of adjusting the artificial viscosity levels, as function of the discontinuities of the pressure ΔP and of the velocity ΔU. This adjustment is made with the intermediary of a parameter α whose value is adjustable between 0 and 1.

$$\vartheta=\alpha\cdot\Delta\mathbf{P}+(1-\alpha)\cdot\Delta\mathbf{U} \tag{5}$$

The total viscosity is a sum of a second-order term in the space ($D2$) preponderant in zones with strong gradients capable of destabilizing the scheme, and a fourth-order term in the space ($D4$) whose role is to diminish the high-frequency numerical instabilities, where ε_2, ε_4, and λ are viscosity terms depending of Equation 5:

$$\mathbf{D2}(\mathbf{U}^n)=\frac{\Delta t}{V(i,j)}\cdot\left[(\Delta x)^2\cdot\frac{\partial}{\partial x}\left(\varepsilon_2\lambda\frac{\partial U}{\partial x}\right)+(\Delta y)^2\cdot\frac{\partial}{\partial y}\left(\varepsilon_2\lambda\frac{\partial U}{\partial y}\right)\right] \tag{6}$$

$$\mathbf{D4}(\mathbf{U}^n)=-\frac{\Delta t}{V(i,j)}\cdot\left[(\Delta x)^4\cdot\frac{\partial^2}{\partial x^2}\left(\varepsilon_4\lambda\frac{\partial^2 U}{\partial x^2}\right)+(\Delta y)^4\cdot\frac{\partial^2}{\partial y^2}\left(\varepsilon_4\lambda\frac{\partial^2 U}{\partial y^2}\right)\right] \tag{7}$$

Then, with Equations 6 and 7, Equations 3 and 4 become

$$\mathbf{U}^{n+1}=(\mathbf{U}^{n+1})_{\text{scheme}}+\mathbf{D2}(\mathbf{U}^n)+\mathbf{D4}(\mathbf{U}^n) \tag{8}$$

Numerical meshing

The calculations were performed on a specific meshing, based on the geometry of the cold-flow experimental setup, at an instant called "Half-combustion" (Plourde 1994). Because of the complex internal geometry, we were led to divide the channel into six discrete domains of calculation that together, formed a grid. This grid was obtained by solving a set of elliptical equations allowing control of the mesh spacing. Three grids were set up to capture significant gradients of the flow (velocity, pressure). The "medium" grid was obtained by retaining one out of two meshes of the fine grid in the two directions of the space. The same procedure was used to obtain the coarse grid from the medium grid. The coarse grid comprising 4110 meshes allowed initiation of the calculations and making them converge toward a steady state. To pass from one grid to a finer one during the calculations, data on the coarser grid were interpolated on the finer one. Finally, study of the unsteady characteristics was carried out on the two finest grids. Table 1 shows the details of the three calculation grids, and the finest grid is described in Figure 2.

A narrowing occurs close to the second obstacle ($X=0.551$) and at the nozzle entrance ($X=0.950$). The throat of the nozzle is situated at $X=0.965$, beyond the diverging part of the nozzle. The mesh sizes at the second obstacle (0.131 mm) and at the throat of the nozzle (0.128 mm) are practically identical, so that

Table 1 Characteristics of the three computation grids

Domain	Grid		
	Coarse	Medium	Fine
1, upper planar channel	1652	6123	23525
2, lower planar channel	1554	5759	21125
3, head-end	98	351	1325
4, second block	350	1287	4925
5, cavity	91	325	1225
6, third block	1092	4043	15525
TOTAL (points)	4837	17888	68650

convergence of the calculations can be optimized. Close to the injection wall, the meshing is tight: the first mesh situated above the wall is located at 0.35 mm with the fine grid and 1.40 mm with the coarse one. Special care was taken to increase the number of meshes in the second numerical domain whose shape was very elongated and that corresponded to the part situated above the top of the obstacle, to describe better the shear layer.

Boundary conditions

Because of the finite volume formulation, with solutions at the centers of the meshes, the borderline values intervene only in the flows at the boundaries. To calculate these flow rates, we used the boundary conditions imposed, completed by the values extrapolated from the field to the borderline. The external borders of the domains corresponding to numerical walls are processed by given boundary conditions (Figure 3a). They could be considered as inert walls, porous walls, or a supersonic downstream borderline. The injection wall is divided into two sections: a horizontal wall and an upright wall upstream of the second obstacle; and a horizontal wall in the downstream part. At half-combustion time, the first block is entirely burnt. Only the second and the third blocks maintain the combustion, simulated here by the injection condition. The calculations are initiated with parameters whose values are based on the experimental

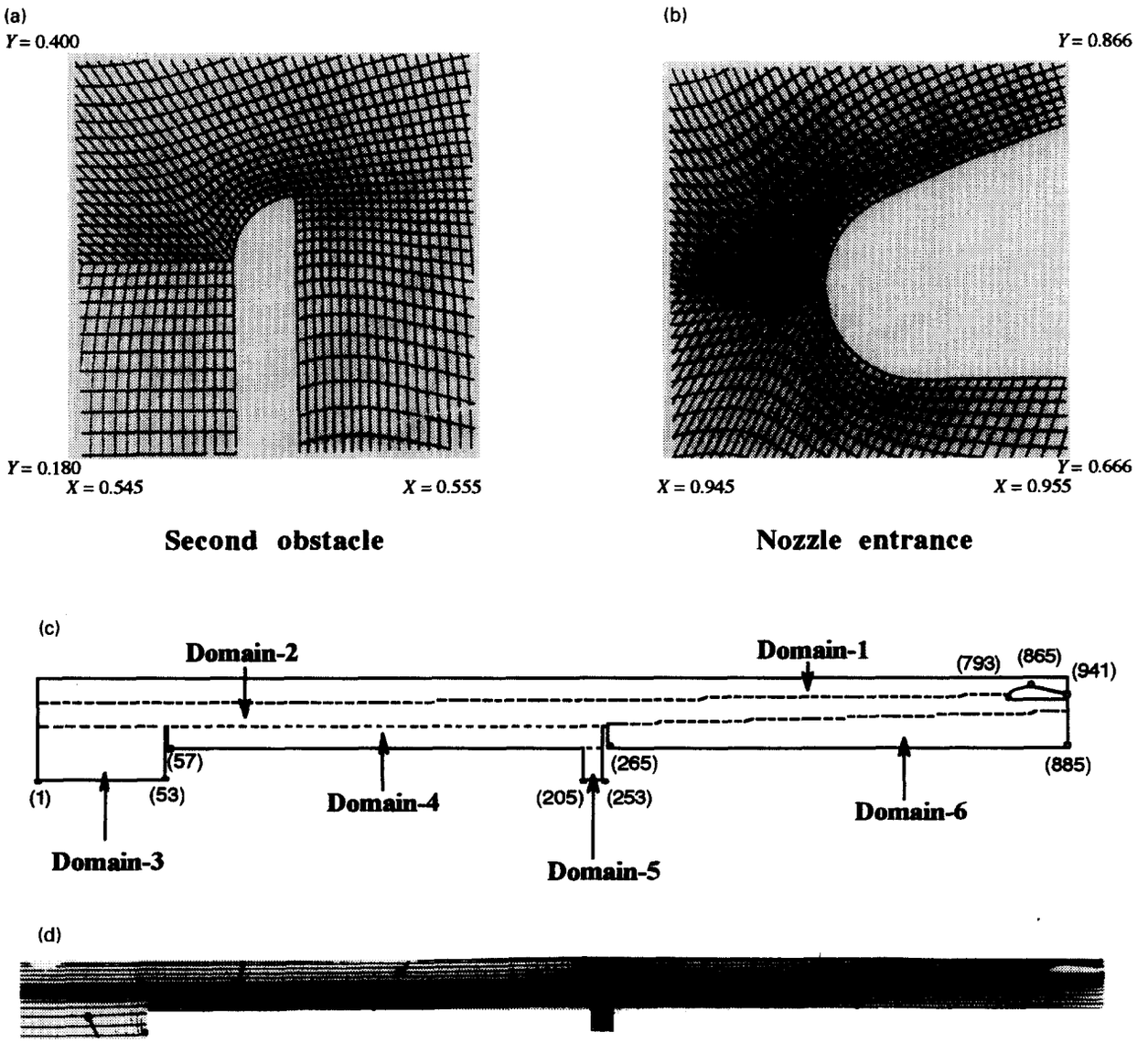

Figure 2 Fine grid description for numerical simulation: a) detail view of the second obstacle region; b) detail view of the nozzle entrance region; c) numeric domains definition; d), overall fine grid description

results. Internal geometry dimensions depend upon aeroacoustic similitude with the full-scale motor; i.e., the conservation of the Mach number and the Strouhal number. Table 2 gives the parameters used.

Mean flow organization

Convergence of calculations—steady state

Calculations were initiated on the coarse grid, starting from steady state at uniform pressure in the chamber ($2.05\ 10^5$ Pa). The criterion of convergence was based on the ratio of emerging mass flow to injection mass flow. This ratio tended toward unity after 100,000 iterative calculation steps, while the residues of the calculations were much reduced. The results obtained on this grid served as initial conditions for further calculations on the medium grid. Four numerical pressure transducers placed at the head-end, normal to the first and the second obstacle, and at the aft-end, allowed us to follow the change of the mean pressure in the whole channel.

The pressure values decrease toward $1.822\ 10^5$ Pa at the head-end, close to the steady state experimental pressure, $1.830\ 10^5$ Pa. After 400,000 iterations on the medium grid, the steady state was established. The Mach number and the pressure maps allowed us to characterize the mean flow behavior. In the upstream part of the channel, before the second obstacle, the variations of these values are small. Figure 4a shows the maps in the downstream part. The iso-Mach lines show there is acceleration of the flow above the obstacle and at the nozzle entrance. At the same time, the isobars generally are normal to the injection surface; moreover, the pressure deviation along the injection wall is low, which proves that the injection is uniform. However, above the obstacle, a disturbance in the pressure field caused by the narrowing of the passage generated by the obstacle itself can be seen. Finally, in the first third and the second half of the downstream zone, two high-pressure zones appear in the middle of a lower pressure zone. These nuclei correspond to the vortex zones made apparent by the isovorticity lines (Figure 4b).

The medium grid allows the calculations to converge toward a steady state. The calculations reveal the presence of a shear layer generated at the top of the second obstacle. At the same time, the development of the flow in the downstream part seems to result from the generating of vorticity structures (Figure 4c and d).

Mean velocity profiles

To improve description of the mean flow, a follow-up of its dynamic change in the channel is conducted. The mean longitudinal velocity profiles are obtained on three grids. On the fine

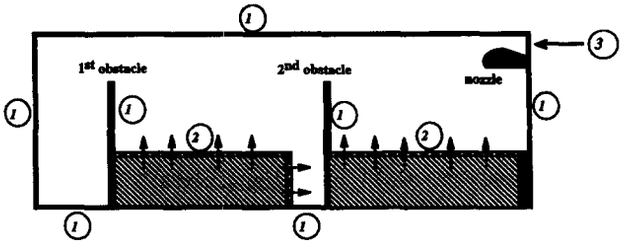

Figure 3 Numerical boundary conditions: ①inert walls; ②porous flow walls—imposed mass flow, fixed temperature, injection velocity normal to the wall with admittance; ③supersonic downstream borderline—free flow with a simple first-order extrapolation

Table 2 Characteristics of the computation parameters

p_{he}, Pa	$1.83\ 10^5$
$\dot{m}$ kg/s	0.066
h_c, m	$28\ 10^{-3}$
h_t, m	$3.08\ 10^{-3}$
L, m	0.623
r J/kg·K	287.7
γ	1.4
T, K	300
a_0, m/s	347.6
kg/m·s	$1.85\ 10^{-5}$
Mean flow Mach number, M	0.067
Strouhal number, St	0.331

grid, the calculations (180,000 iterations) are performed from the final state given by the medium grid. These profiles obtained in different sections show the specific organization of the flow upstream and downstream of the second obstacle (Figure 5).

Upstream of the obstacle at $X = 0.151$, the longitudinal velocity increases from the injection wall ($Y = 0$) to close to the upper wall ($Y = 0.80$) where it reaches a maximum value; it is equal to zero along this wall. The flow rate accelerates from the first obstacle, where the mass injection begins, until the second obstacle. This acceleration is generated by the wall mass transfer. The average velocity at $X = 0.151$ is close to 0.5 m/s, while it reaches 4.5 m/s in the section defined by $X = 0.343$. The steady state is not well established on the coarse grid, with the result that the mean longitudinal velocity profiles are slower than on the two other grids, where the profiles are practically identical, with the deviation not greater than 5% of the calculated velocity. Upstream, the profiles show that there is always a laminar regime in spite of axial (Re_a) and injection (Re_i) Reynolds numbers of high values. These profiles agree with Taylor's classical theoretical profiles (Taylor 1956) obtained for a case free of discontinuities. Comparison with the experimental results shows that there is a slight overestimation of the experimental data of a few cm/s; e.g., $X = 0.343$, the maximum on the numerical grid is close to 8.90 m/s but reaches 8.55 m/s experimentally.

The passage of the obstacle at $X = 0.551$ (the seat of a significant narrowing of the passage and of the encounter of two flows of different directions and velocities) is the site of strong shearing. On the velocity profiles, significant transversal gradients, the presence of inflexion points, and the appearance of overspeed can be noticed. The average velocity in this section is close to 16 m/s, with a maximum of 19.16 m/s reached 2 mm below the upper wall. The particularity of this profile is the appearance of high-velocity gradients just at the top of the obstacle ($Y = 0.321$) at a height δ estimated at 1.6 mm. The velocity deviation Δu_e is 5.53 m/s along the distance δ; i.e., 30% of the mean velocity in this section. The overspeed of 13.01 m/s is located at $Y = 0.382$. The transversal velocity component is also submitted to a strong velocity gradients at the top of the obstacle. It demonstrates the existence of a strong shearing of the flow at the top of the obstacle.

Computations on the fine grid show some differences from those on the medium grid. The overspeed is higher by 0.31 m/s, and the velocity deviation is smaller on a thinner layer δ about 0.62 mm. This shows that the profiles are affected by the meshing but only in the overspeed zone. Table 3 presents the characteristics of the shear layer obtained in the three grids, and they are compared with the experimental results. The fine grid gives a better description of the shear layer: the shear-layer thickness in the fine grid is identical with that of the experimental measurements.

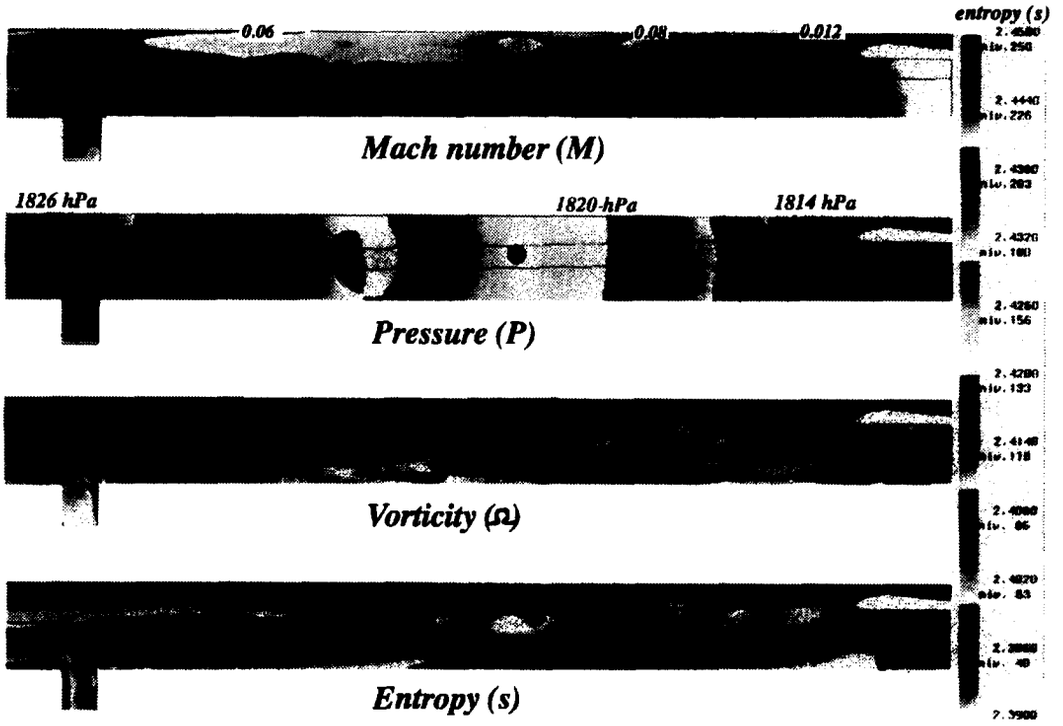

Figure 4 Mach number, pressure, vorticity, and pseudoentropy maps on medium grid: a) iso-Mach number lines; b) isopressure lines; c) isovorticity lines; d) isopseudo entropy lines

Just at aft-end of the obstacle, $X = 0.555$, the profile is again characterized by a more significant overspeed of about 13% in relation to the obstacle. The overspeed position allows us to obtain two zones: the lower part ($Y < 0.321$) for which u is equal to zero; the flow emerging from the injection wall is mainly transversal. The upper part ($Y > 0.321$) presents a significant acceleration and strong velocity gradients but weaker than in the passage section created by the obstacle. More aft, at $X = 0.720$, the disappearance of the overspeed can be seen. The injection downstream tends to cancel the effect of the obstacle: the mass injected by the porous wall contributes to the total acceleration of the flow rate between $X = 0.720$ to $X = 0.912$, increasing the mean velocity by about 25%. Finally, downstream of the obstacle, the flow is significantly disturbed when passing the obstacle. It reorganizes itself, and a strong acceleration can be observed in the aft-end region of the last block. The numerical profiles are in agreement with the experimental profiles on the two finest grids.

Hydrodynamic instability characterization

Analysis of the unsteady pressure field

Once the steady-state solution has been found, numerical transducers are located on certain meshes to follow the change over time of the velocity and the pressure at different zones of the chamber. Eight pressure transducers are placed either inside the chamber or on the upper wall (see Figure 6 for transducer locations). Then, medium and fine grids are used to proceed with the computations starting at the same initial moment.

The signal recorded for the medium grid lasts 53.6 ms—long enough for studying its spectral content. At head-end, p_{he} is estimated at 1.822 10^5 Pa, and the spatial decrease of mean pressure between the head-end and the nozzle entrance is close to 0.031 10^5 Pa; i.e.a, 1.7% of p_{he}, which confirms the hypothesis of a subsonic internal flow. Moreover, time fluctuations of the mean pressure are noticed: the unsteady pressure amplitude is relatively small (average 85 Pa along the whole channel with a maximum at the nozzle entrance) as compared to the mean pressure, and represents about 1/2000 of p_{he}, which is not negligible. The unsteady fluctuations seem to be systematic and periodic, because the spectral analysis gives the characteristics frequencies (Figure 7a) and show an unstable activity close to the first longitudinal acoustic modes (theoretical values: f_{1L} = 278 Hz, $f_{2L} = 577$ Hz, $f_{3L} = 836$ Hz, $f_{4L} = 1115$ Hz, and f_{5L} = 1393 Hz). The highest peak, close to 530 Hz, is present in all the spectral densities. This peak particularly dominates at the head-end, in midchamber, and at the nozzle entrance. The 260 Hz peak with its very small amplitude in the upstream part, is definitely higher downstream of the obstacle, especially at the nozzle entrance, where its amplitude reaches two-thirds of the second mode amplitude. Therefore, the acoustic of the chamber is excited by the flow generated by injection.

The phenomenon of acoustic resonance can be attributed to the coupling between the instabilities generated at the top of the obstacle and the internal acoustic field. The resonance seems to favor the frequency at 527 Hz, corresponding to f_{2L} acoustic mode. Figure 7b shows the results of the analysis of experimental, unsteady pressure signals. The change of the spectral pressure density shows that the first mode is preponderant at the head-end, and at the aft-end; whereas, the second mode is the more significant mode at the second obstacle. Amplitudes of the peaks are different, but resonance of the channel is numerically as it was experimentally.

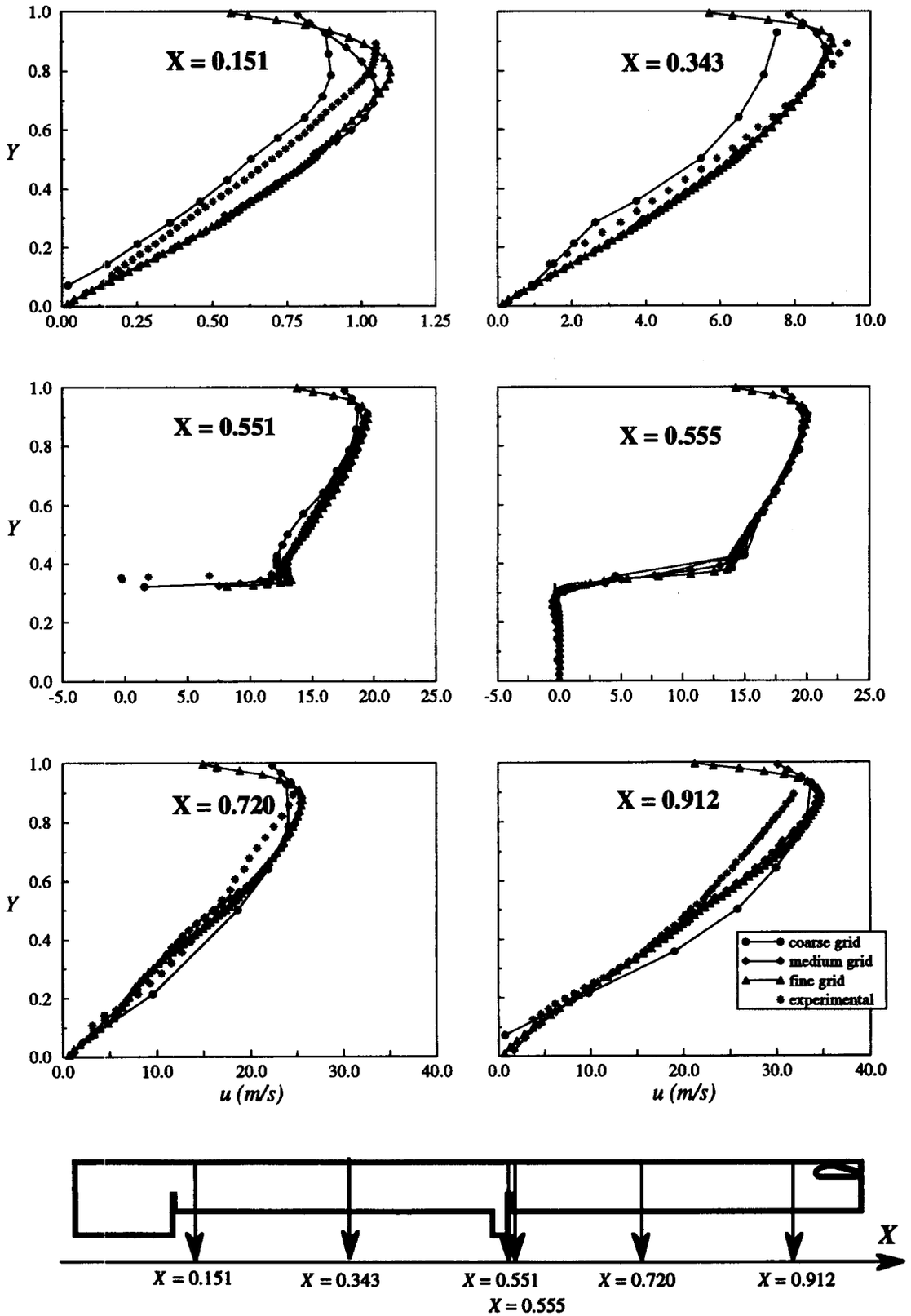

Figure 5 Mean velocity profiles of the longitudinal component—comparison of numerical profiles for three grid refinements to experimental profiles

Table 3 Characteristics of the shear layer

	Numerical			
	Coarse grid	Medium grid	Fine grid	Experimental
u_{max}, m/s	12.35	13.01	13.32	13.01
Δ_{u_e}, m/s	10.81	5.53	5.18	6.64
δ, mm	1.75	1.62	0.62	0.60

Vortex-shedding phenomenon

Extra computations are carried at constant time steps equal to 1/140,000 of 527 Hz frequency signal period, noted T_{527}. The computation results also are stored at regular intervals of time, corresponding to T_{527}. These extra calculations are made over six periods of T_{527} equal to 11.40 ms, which allow us to define seven moments of computation. At each of these moments, the pressure field is determined, and the entropy and the vorticity in each mesh of the grid are calculated. It is then possible to draw the maps obtained in the whole chamber. The variations, upstream of the second obstacle, are even negligible, so the maps are described only from the flowing cavity upstream of the obstacle to the extremity of the channel ($0.5 < X < 1.0$); i.e., the downstream zone.

The pressure field (Figure 8a) change shows there is a beat of the isobars and confirms the appearance of a strong pressure zone surrounded by lower pressure areas. These nuclei seem to correspond to vortices whose presence is manifested by the isoentropy lines (Figure 8b). Indeed, this entropy shows that a shear layer is created at the top of the obstacle, generating structures whose dimensions increase at the rear region. A pairing seems to become apparent in the middle part of the third block: two structures grow spatially and fill over half of the channel's height before the two structures move closer to combine upstream of the nozzle entrance.

A more precise characterization of the spatial and temporal development of the structures is allowed by the change of the isovorticity lines (Figure 8c). From the spatial point of view, these lines confirm the observation made in Figure 4: the vorticity structures are created at the top of the obstacle, where the shearing constraints are very intense. These instabilities develop downstream and particularly in the second numerical domain. The eddies are concentrated in the upper part of the channel close to the nozzle entrance, creating a zone without vortices below the submerged nozzle. From the temporal point of view, the release of whirls occurs downstream of the top of the obstacle between each image; i.e., at 527 Hz. These structures combine. Therefore, the preponderance of the peak at 527 Hz on the pressure spectra can be attributed to the vortex shedding. However, from the middle of the downstream block, joining of two structures that pair off by a rotational movement combine in the rear part. This pairing phenomenon generates a reduction by a factor of 2 of the emission frequency. Indeed, Figure 8c demonstrates this pairing every second image; i.e., that is periodic with a 260 Hz frequency. Therefore, the analysis of the isovorticity lines allow quantification of the vortex shedding and the pairing of the instabilities in the downstream zone.

Good correspondence between hydrodynamic instability frequencies and acoustic modes strengthens the hypothesis of a hydroacoustic coupling. Complementary information is given by the computation of Fourier complex coefficients linked to the pressure field.

$$CF(\mathbf{p}) = \frac{2}{nT} \cdot \int_{to}^{to+nT} \mathbf{p}(t) \cdot \exp(-i\omega t) \cdot dt$$

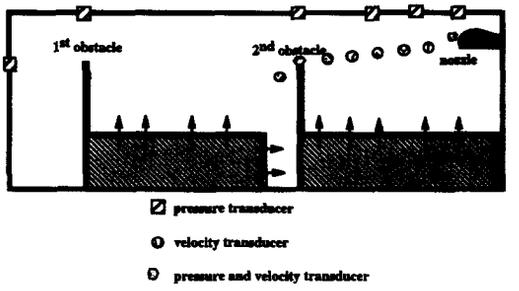

Figure 6 Numerical pressure and velocity transducer locations

where

$$T = \frac{1}{f}, \text{ with } f = 527 \text{ Hz} \quad \text{and} \quad n = 6 \tag{9}$$

These coefficients are calculated over six periods of T_{527} and on the second resonance mode of the channel. Figure 9 presents the variations of the module and the phase of $CF_{(p)}$ along the upper wall. With this curve, the localization of the vortex-shedding is obvious. The shape of the steady state wave shows there are two discrete zones, each characterized by a spatial wave number. The classical character of the pure acoustic wave can be observed in the upstream part of the chamber, between $X = 0$ to $X = 0.551$, where two maxima are situated at the forward part and in the middle of the channel, as well as a maximum situated in the first quarter of the chamber. The aspect of the wave in the part downstream from the second obstacle is the result of the composition of two waves of equal frequency propagating at different velocities. The first wave is the acoustic wave moving at sonic speed a_0 generating a minimum at $X = 0.750$ and a maximum at aft-end. The second wave, linked to the vorticity, moves exactly at the speed of the vortices, less rapid than sonic speed. From $X = 0.551$, we can observe the variations of the $CF_{(p)}$ module and phase that characterize the effect of the vortices on the acoustic wave; the phase changes from -180 to $+180°$ when a vortex passes, with less frequency when the pairing occurs. Figure 9b illustrates this change in the whole chamber. It shows the troughs and the crests of the pressure curves situated, respectively, at head-end, upstream of the second obstacle, and at aft-end, for the crests, and at the first- and third-fourths of the channel for the troughs. It confirms that in the downstream domain, the vorticity structures actually disturb the acoustic field; circular zones characterizing vortices modify the change of the field.

Analysis of the eight velocity signals (see Figure 6 for the transducer locations) confirms the unsteady dynamic flow behavior. Upstream of the obstacle, the velocity fluctuations are feeble, about 2% of the mean velocity in the section under consideration ($X = 0.543$); whereas, downstream, where the shear constraints are stronger, these fluctuation levels increase significantly. The local turbulence rate τ_u is over 15% in the downstream region determined by the shear layer. Spectral analysis of these velocity fluctuations shows the preponderance of the first two longitudinal modes (Figure 10). In the downstream part close to the second obstacle, particularly $X = 0.659$, the spectra are dominated by the frequency of 527 Hz illustrated by a very narrow peak. The farther away from the obstacle, with increasing values of X, the greater the increase of the peak at 260 Hz between $X = 0.642$ and $X = 0.738$, where the amplitude becomes equal to that of the second mode: it is precisely here that the

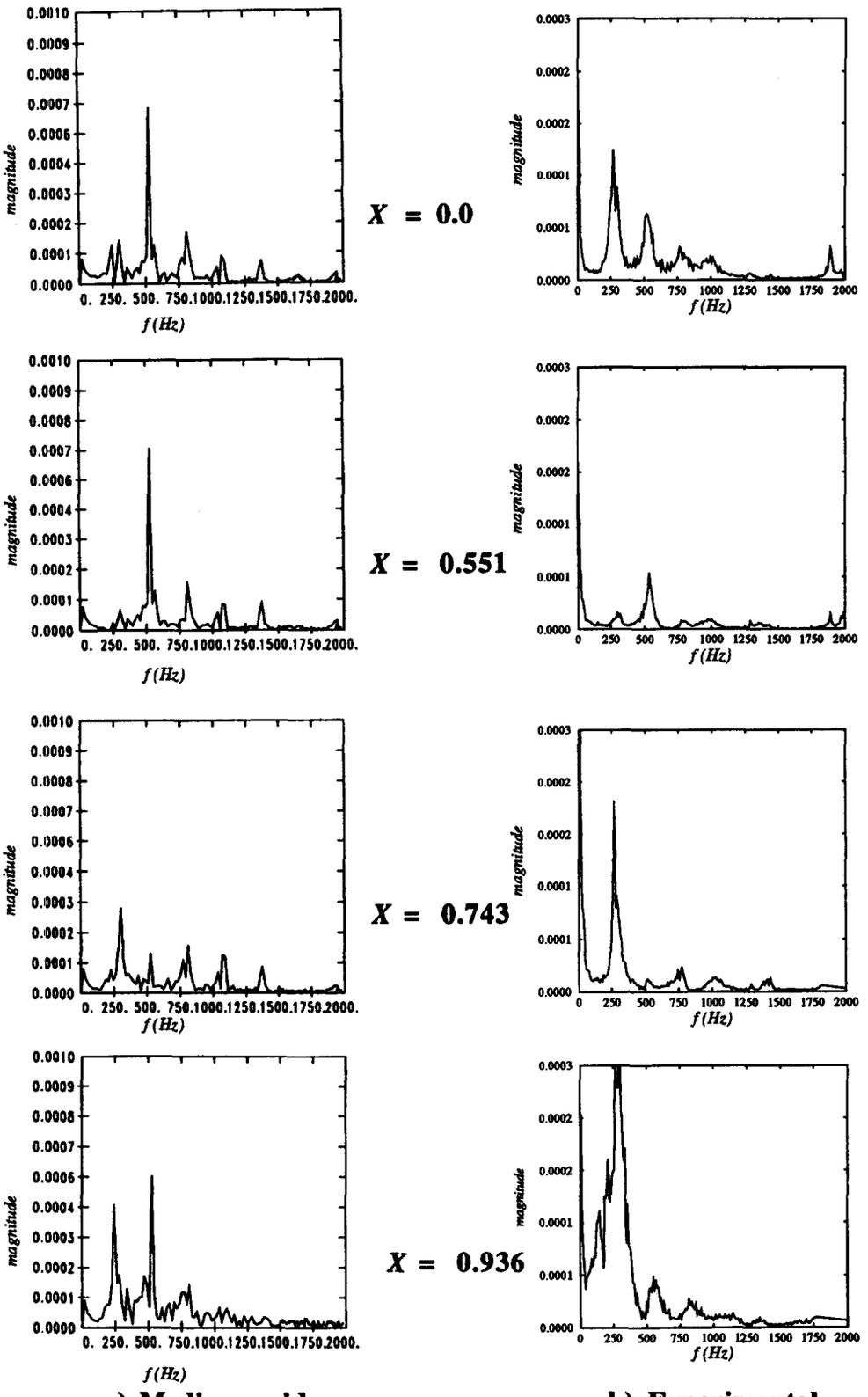

Figure 7 Pressure signal spectra: a) medium grid; b) experimental

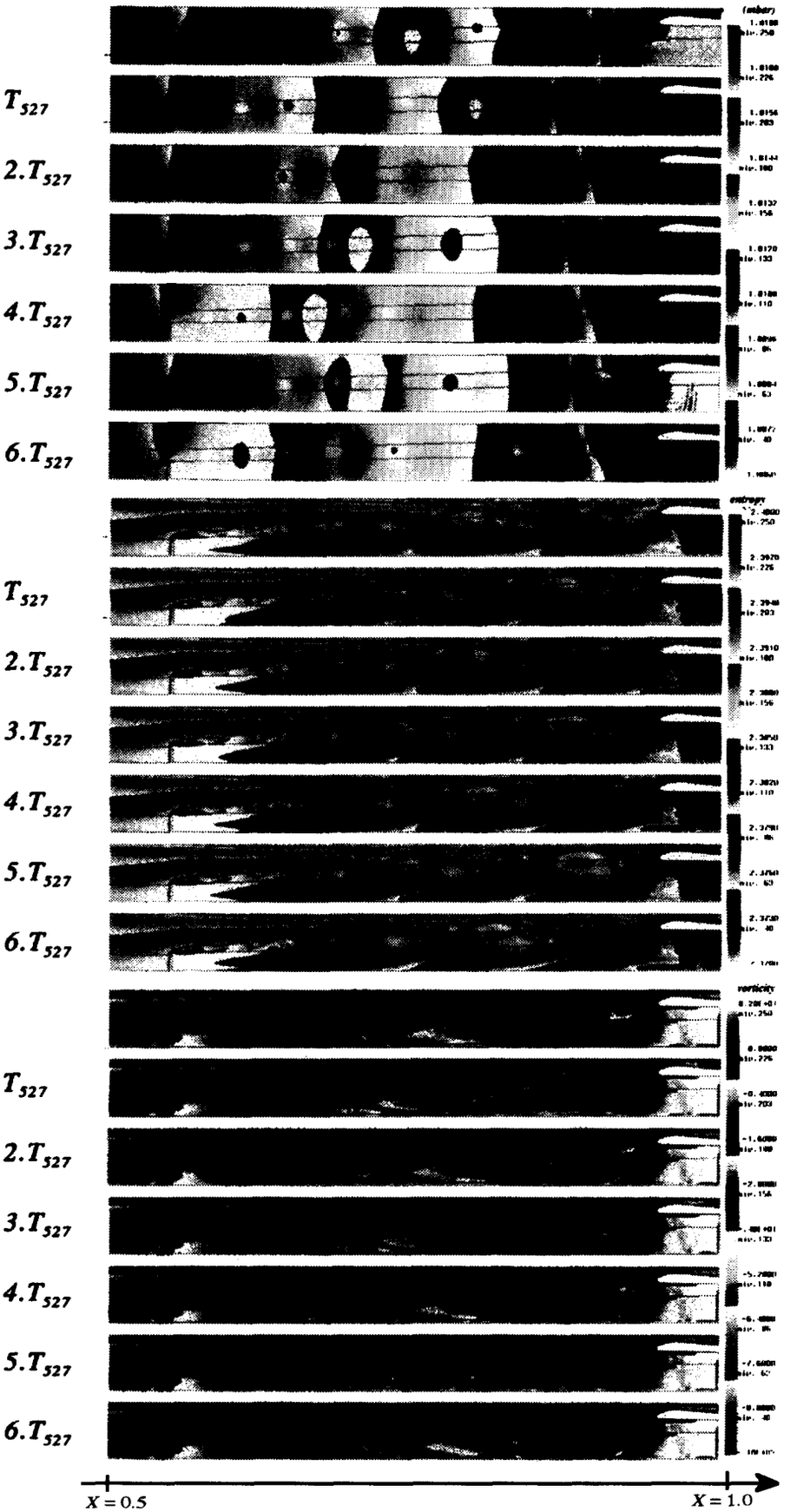

Figure 8 Internal isopressure a), isoentropy; b) and isovorticity; c) lines over six periods of f_{2L}, medium grid

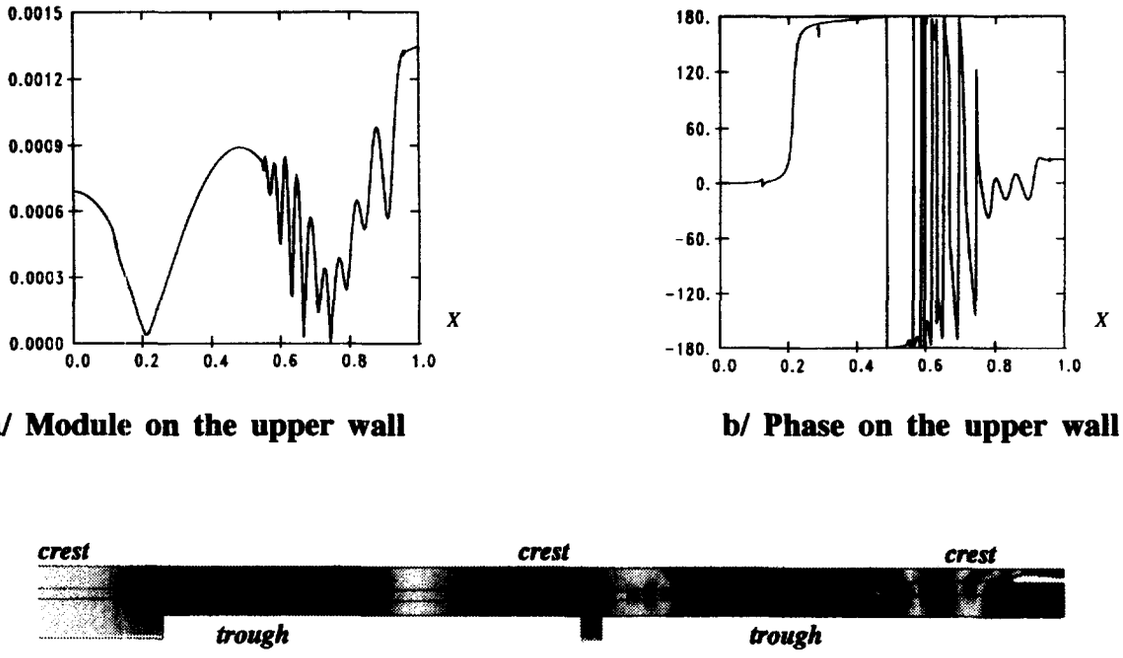

Figure 9 Change of the module and the phase of pressure complex Fourier coefficients corresponding to the second acoustic mode; medium grid: a) on the upper wall; b) internal

pairing occurs. From $X = 0.834$, the spectrum is dominated only by the first longitudinal mode. Spectral analysis confirms that the vortex-shedding and the development of these structures in the downstream zone are linked to the first two modes of the channel and that there is a coupling between the hydrodynamic and the acoustic fields.

Influence of the meshing

There is very little, or even no, influence of the grid on the iso-Mach lines or on the isobars. That is why they have not been reported. On the other hand, the influence can be clearly observed on the vorticity fields. Qualitatively, comparable results were obtained in steady state on the medium and fine grids in the mean pressure and velocity fields. There is a difference only in the dynamic description of the shear layer at the top of the obstacle ($X = 0.551$). The fine grid, more accurate, allows us to describe better the characteristic velocity profiles (Figure 6), particularly because the decrease of the mesh size at the top and downstream of the obstacle allows us to capture better the longitudinal and transversal velocity gradients.

On the other hand, the description of the unsteady state shows some differences. Passing from the medium grid to the fine grid, the levels of fluctuations of the pressure and the velocity increase by a factor of 1.5 to 2.0. In particular, the level of pressure fluctuation at head-end increases by 1.53, to reach 130 Pa in the fine grid. Apparently, the instability levels are reinforced on the finer grid. In both cases, however, the levels of pressure compared to those obtained experimentally are overpredicted: the experimental results give the mean value of 36 Pa for the whole chamber. This numerical overestimation can be attributed to the boundary conditions of the injection wall. Acoustically, the injection wall is considered as a wall reinforcing the acoustic resonance conditions, although tests show experimentally that wall admittance is estimated at 0.87 under nominal conditions of pressure and injection mass rate. In the case of velocity fluctuations, the experimental levels correspond to those obtained with the fine grid. For instance at $X = 0.629$ and $Y = 0.393$, τ_u reaches 22.05% on the medium grid, but 30.78% on the fine grid. Experiments with a laser-Doppler-anemometer (LDA) give an experimental rate of 30.98%. Generally, velocity fluctuation levels on the fine grid agree well with experimental results.

However, spectral analysis of the pressure fluctuations (Figure 11a) confirms that the frequencies of acoustic resonance are close to the first two longitudinal modes. Spectral analysis of the velocity signals confirms the coupling between the hydrodynamic instabilities and the acoustic field (Figure 11b). These computations give credence to the fact that vortex-shedding is the phenomenon that pilots the instabilities, as is the case with the medium grid. However, it can be seen that the spectra, if they make the first two longitudinal modes predominant, do not present the same change in the downstream zone. The second mode remains the dominant mode at the top of the obstacle and just behind it, and it rapidly has a smaller amplitude. The first mode becomes the dominant peak at $X = 0.642$, as against $X = 0.834$ in the medium grid: a sensitivity to the meshing is observed. This sensitivity is especially marked on the vorticity field. Figure 12 shows the isovorticity lines obtained over six periods of T_{527}. Compared with the medium grid, the temporal point of view is not modified: vortices are shed at 527 Hz, and the pairing occurs at 260 Hz. On the other hand, the spatial change is apparently affected: 1) the sizes of the structures are smaller, because the meshes are smaller and the $(\partial v/\partial x)$ and $(\partial u/\partial y)$ velocity gradients are closer to the experimental results; 2) structure pairing occurs sooner in the chamber—two structures combine at the third of the downstream zone. The early pairing allows us to explain the predominance of the first longitudinal mode starting at the middle of the downstream zone as described by the velocity spectra.

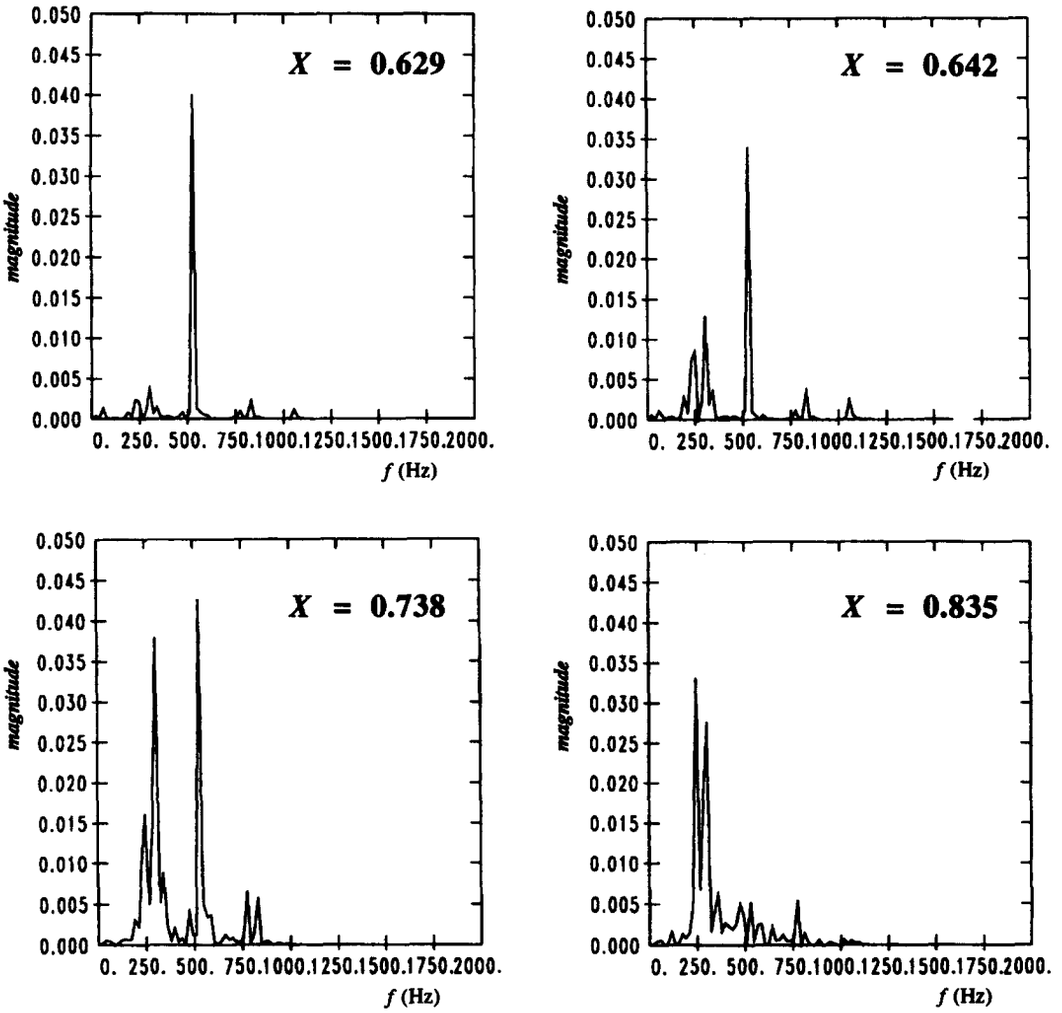

Figure 10 Unsteady longitudinal velocity fluctuations spectra, medium grid

Therefore, the instabilities are not sensitive temporally to the meshing, but their development in space depends upon the size of the computation meshes. The fine grid reinforces the process of acoustic coupling and seems to accelerate the structure pairing. Last, the fine grid results, especially the description of the shear layer, from a dynamic angle and the change of pressure and velocity spectrum tends to reinforce the idea that the simulation in a fine grid gives results that are in better agreement with the cold-flow experimental investigation. Visualization conducted on the experimental setup shows that structures are created at the top of the obstacle and develop downstream of the obstacle, as predicted by the fine grid calculations.

Conclusions

The computations we present here correspond to a cold-flow simulation of a solid segmented propellant rocket motor. The wall injection generates a particular development of the flow inside the complex internal geometry of the chamber. The second obstacle determines three zones. The upstream part of the channel presents a laminar flow that constitutes the main flow that impinges against the second obstacle. The top of the obstacle is the seat of a strong shearing and vortex generation in its wake, accompanied by a substantial turbulent activity. The downstream part corresponds to the zone of the development of the vortex structures. These hydrodynamics instabilities are in accordance with the first two longitudinal modes of the chamber: the vortex-shedding is connected to the second mode, while the pairing occurs on the first mode. Therefore, a coupling of the characteristic flow phenomenon and the chamber acoustics is verified. Last, the spatial development of the instabilities is sensitive to the grid meshing: the finest grid accelerates the vortex pairing and reinforces the hydroacoustic coupling. The numerical approach is compared with the experimental investigation. The steady state numerical results are in good agreement with the experiments. The numerical approach tends to overestimate the experimental unsteady flow behavior, but it is described better by the finest grid.

Our results advance development in the field. They allow to bring elements of response concerning the grade of representation of calculations to simulate a cold-flow experimental investigation in the case of a segmented solid propellant rocket motor. Moreover, this work contributes to understanding the behavior of the flow generated by injection through a porous wall in a channel.

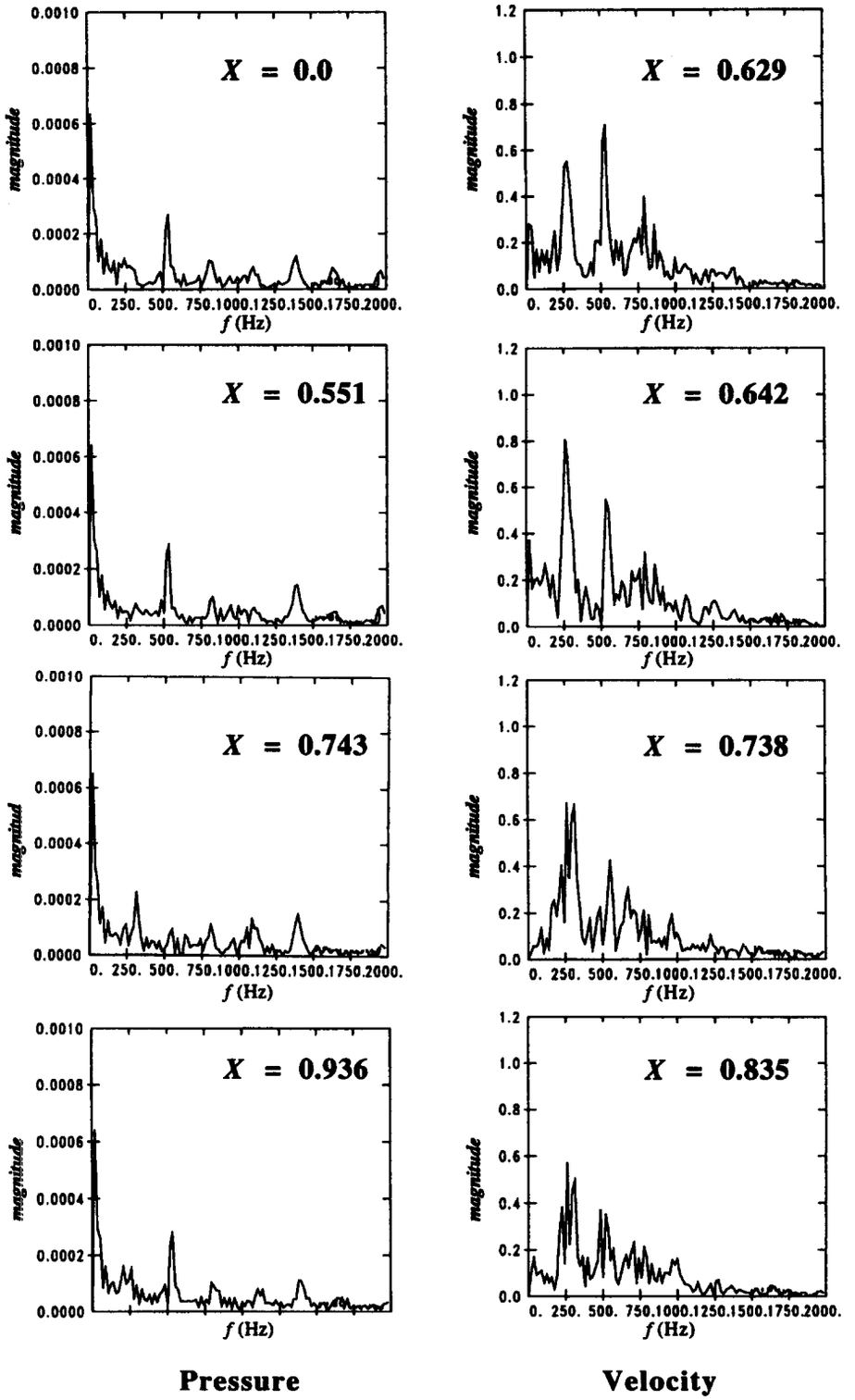

Figure 11 a) Spectra of surface pressure; b) longitudinal velocity fluctuations, fine grid

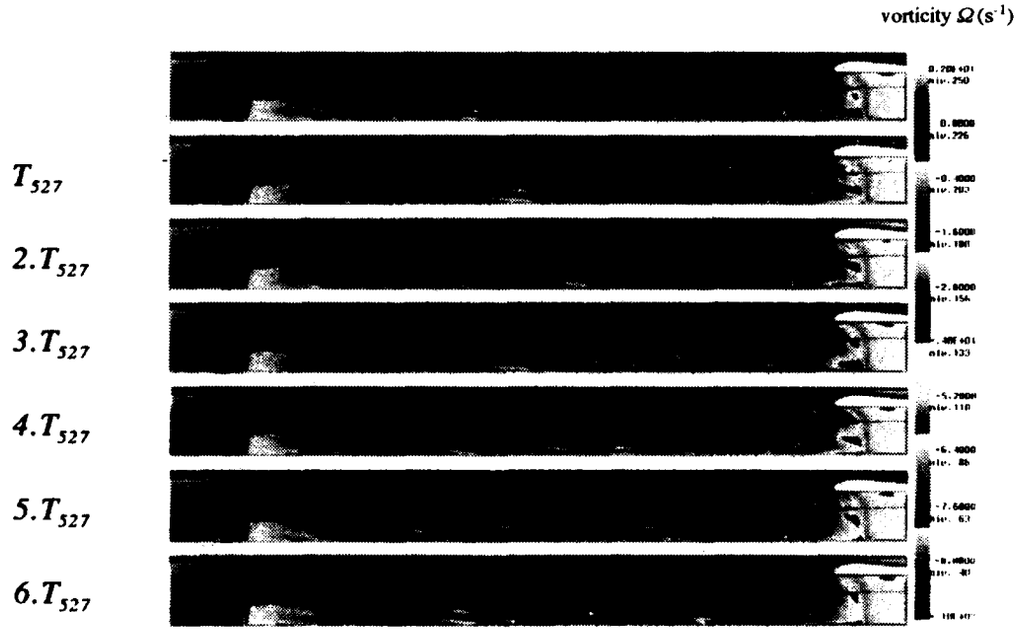

Figure 12 Change of isovorticity lines over six periods of f_{2L}, fine grid

Acknowledgments

We thank the CNES/DLA for their financial support and in particular Messers. Bec and Robert for their help. This research was performed under the Aerodynamics of Solid Segmented Motors program of the CNES, concerning the MPS-P230 of ARIANE 5. We also thank N. Lupoglazoff of the ONERA for his aid and his pertinent remarks.

References

Brown, R. S., Dunlap, R., Young, S. W., and Waugh, R. C. 1985. Vortex-shedding studies in a simulated coaxial dump combustor. *J. Propulsion*, **1**, 413–415

Culick, F. E. C. and Magiawala, K. 1979. Excitation of acoustic modes in a chamber by vortex-shedding. *J. Sound Vibration*, **64**,

Dunlap, R. and Brown, R. S. 1981. Exploratory experiments on acoustic oscillations driven by periodic vortex-shedding. *AIAA J.*, **19**, 408–410

Dunlap, R., Blackner, A. M., Waugh, R. C., Brown, R. S., and Willoughby, P. G. 1990. Internal flow field studies in a simulated cylindrical post rocket chamber. *J. Propulsion*, **6**, 690–704

Flatau, A. and Vanmoorhem, W. K. 1990. Prediction of vortex-shedding responses in segmented solid rocket motors. *Proc. AIAA/SAE/ASME/ASEE 26th Joint Propulsion Conference*, (Orlando, FL, July 16–18)

Hourigan, K., Welsh, M. C., Thompson, M. C., and Stokes, A. N. 1990. Aerodynamic sources of acoustic resonance in a duct with buffles. *J. Fluids Structures*, 345–370

Isaacson, L. K. and Marshall, A. G. 1982. Acoustic oscillation in internal cavity flows: Non-linear resonant interactions. *AIAA J.*, **20**, 152–154

Jameson, A., and Schmidt, W. 1981. Numerical simulation of the euler equations by volume methods using Runge–Kutta time steps schemes. AIAA 14th Fluid and Plasma Dynamic Conference (Palo Alto, CA, June).

Mason, D. R., Folkman, S. L., and Behring, M. A. 1970. Thrust oscillations of the space shuttle solid rocket booster motor. *Proc. AIAA 15th Joint Propulsion Conference*, (Las Vegas, NV, June 18–20), AIAA, New York, Paper 79-1138

Mathes, H. B. 1980. Assessment of chamber pressure oscillations in the shuttle solid rocket booster motor. *Proc. AIAA/SAE/ASME 16th Joint Propulsion Conference*, Hartford, CT, June 30–July 2), AIAA, New York, Paper 80-1091

Plourde, F. 1994. Structures turbulentes d'un écoulement segmenté à injection pariétale, Ph.D. thesis, University of Poitiers, Poitiers, France

Scippa, S., Pascal, P., and Zanier, F. 1994. Ariane 5-MPS-chamber pressure oscillations full-scale firings results analysis and further studies. *Proc. AIAA 30th AIAA/ASME/SAE/ASEE Joint Propulsion Conference*, (Indianapolis, IN, June 27–29)

Taylor, G. I. 1956. Fluid flow in regions bounded by porous surface. *Proc. Royal Soc. London*, **234A**, 456–475

Vuillot, F. and Lupoglazoff, N. 1991. Two-dimensional numerical simulation of the stability of a solid propellant rocket motor. *Proc. AIAA 29th Aerospace Sciences Meeting*, (Reno, NV, Jan. 7–10), AIAA, New York, Paper 91-0205

Vuillot, F. and Lupoglazoff, N. 1992. Numerical simulation of vortex-shedding phenomenon in 2-D test case solid rocket motors. *Proc. AIAA 30th Aerospace Sciences Meeting*, (Reno, NV, Jan. 6–9, AIAA, New York, Paper 92-0776

Vuillot, F. and Lupoglazoff, N. 1993. Comparison between firing tests and numerical simulation of vortex-shedding in a 2-D test solid motor. *Proc. AIAA 24th Fluid Dynamics Conference*, (Orlando, FL, July 6–9), AIAA, New York, Paper 93-0776